Nanoscale

Group 13 Lewis Acid Catalyzed Synthesis of Metal Oxide Nanocrystals via Hydroxide Transmetallation

Journal:	*Nanoscale*
Manuscript ID	NR-ART-04-2021-002397.R1
Article Type:	Paper
Date Submitted by the Author:	17-Jun-2021
Complete List of Authors:	Gibson, Noah; Auburn University, Chemistry and Biochemistry Bredar, Alexandria; Auburn University, Chemistry and Biochemistry Chakraborty, Nilave; Auburn University, Chemistry and Biochemistry Farnum, Byron; Auburn University, Chemistry and Biochemistry

Group 13 Lewis Acid Catalyzed Synthesis of Metal Oxide Nanocrystals via Hydroxide Transmetallation

Noah J. Gibson†, Alexandria R. C. Bredar†, Nilave Chakraborty, Byron H. Farnum*

Department of Chemistry and Biochemistry, Auburn University, Auburn, AL 36849

*corresponding author

†Equal Contribution

Abstract

A new transmetallation approach is described for the synthesis of metal oxide nanocrystals (NCs). Typically, the synthesis of metal oxide NCs in oleyl alcohol is driven by metal-based esterification catalysis with oleic acid to produce oleyl oleate ester and M-OH monomers, which then condense to form M_xO_y solids. Here we show that the synthesis of Cu_2O NCs by this method is limited by the catalytic ability of copper to drive esterification and thus produce Cu^+-OH monomers. However, inclusion of 1-15 mol% of a group 13 cation (Al^{3+}, Ga^{3+}, or In^{3+}) results in efficient synthesis of Cu_2O NCs and exhibits size/morphology control based on the nature of M^{3+}. Using a continuous-injection procedure where the copper precursor (Cu^{2+}-oleate) and catalyst (M^{3+}-oleate) are injected into oleyl alcohol at a controlled rate, we are able to monitor the reactivity of the precursor and M^{3+} catalyst using UV-visible and FTIR absorbance spectroscopies. These time-dependent measurements clearly show that M^{3+} catalysts drive esterification to produce M^{3+}-OH species, which then undergo transmetallation of hydroxide ligands to generate Cu^+-OH monomers required for Cu_2O condensation. Ga^{3+} is found to be the "goldilocks" catalyst, producing NCs with the smallest size and a distinct cubic morphology not observed for any other group 13 metal. This is believed to be due to rapid transmetallation kinetics between Ga^{3+}-OH and Cu^+-oleate. These studies introduce a new mechanism for the synthesis of metal oxides where inherent catalysis by the parent metal (*i.e.* copper) can be circumvented with the use of a secondary catalyst to generate hydroxide ligands.

Introduction

The colloidal synthesis of nanocrystalline solids is a highly active area of research given that many nanocrystalline materials have unique properties for applications in optical, photochemical/photocatalytic, and electrochemical/electrocatalytic fields.[1,2] The synthetic methods developed for these materials often involve a high level of control on the composition, morphology, and size of the nanocrystals (NCs) generated.[2,3] The most investigated methods have been based on heat-up or hot-injection procedures toward the synthesis of metal chalcogenide semiconductors.[4,5] Each method operates under similar principles where the reaction of precursor molecules with a solvent and a surfactant leads to a nucleation event followed by NC growth, as described by the LaMer mechanism[6], although more recently the theory of NC growth has been expanded due to the complexities of the precursors and reaction environments.[7]

The hot-injection method relies on a fast injection of precursor molecules into the reaction solution and requires rapid reactivity of the precursor to ensure a single nucleation event. However, the scale-up of the synthesis is challenging because of its reliance on uniform mixing to achieve a single nucleation event and homogeneous cooling of the reaction to separate nucleation and growth. The heat-up synthesis method does not suffer from these setbacks because all reaction components are present upon heating of the reaction, simplifying issues with scale-up. However, secondary nucleation events are more likely to occur because of sustained monomer generation, which can overlap the growth and nucleation stages of the reaction, broadening nanocrystal size.

More recently, a continuous-injection method has been developed for metal oxide NCs and has shown great promise for controlled generation of a wide variety of materials.[8] While both the hot-injection and continuous-injection methods introduce precursor molecules to a pre-heated reaction solution, the continuous-injection is performed with a slower, controlled injection rate such that addition of the entire precursor volume can take multiple minutes to achieve. Instead of rapid nucleation and growth observed during fast hot-injection, the continuous-injection method allows for a layer-by-layer growth of NCs and fine control of size, morphology, and doping.[8–12]

For the synthesis of metal oxides, the reaction proceeds via metal-catalyzed esterification of long-chain carboxylic acids with long-chain alcohols to produce the corresponding ester and metal hydroxide (M-OH) monomers (**Scheme 1**, top), which then condense to form metal oxide NCs. The successful synthesis of nanocrystals using the continuous-injection method relies on the ability of the precursor metal to catalyze the esterification reaction to form M-OH in addition to the

proclivity of M-OH monomers to undergo condensation to form a metal oxide. A wide variety of metal oxide NCs have been synthesized with this method, including In_2O_3, CoO, Mn_3O_4, Fe_2O_3, and ZnO.[8,13–15] The doping of In_2O_3 with different metals (*e.g.* Sn:In_2O_3) and the generation of core-shell NCs have established the versatility of this method.[8–10,16]

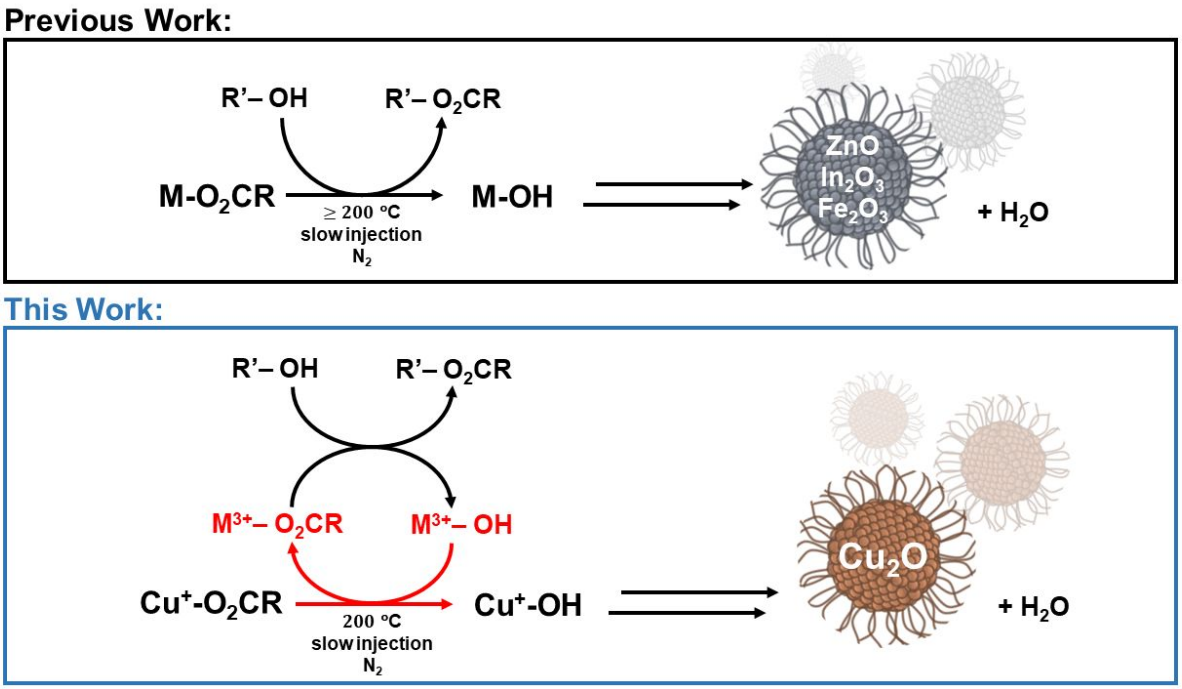

Scheme 1. Reaction schemes for metal oxide NC synthesis. (top) Metal oleate (M-O_2CR) catalyzed esterification produces metal hydroxide (M-OH) monomers which undergo condensation to form metal oxide NCs. (bottom) Synthesis of Cu_2O NCs is achieved through an alternative catalytic route in which esterification by a group 13 metal cation results in transmetallation of hydroxide ligands from M^{3+}-OH to produce Cu^+-OH monomers.

Despite the wide range of accessible materials, Ito *et. al.* previously found that NCs consisting of antimony, copper, and silver could not be produced using the continuous-injection method.[8] This is seemingly due to the inability of these metals to catalyze the necessary esterification reaction to form M-OH monomers. This indicates that more research is needed to understand the different catalytic rates of metals toward esterification and the types of NCs they generate.

Here, we report the direct synthesis of Cu_2O NCs smaller than 100 nm using the continuous-injection method. The key to our approach is the presence of catalytic amounts (1-15 mol%) of Al^{3+}. Ga^{3+}, or In^{3+} cations. The introduction of non-incorporative cations and inorganic complexes has been explored for the synthesis of metal chalcogenide[17–19] and metal oxide[11] NCs; however,

the addition of these species has been reported to change the resultant NC morphology and not necessarily impact the reactivity of metal precursors. We find that addition of group 13 cations to our system specifically enhances the reactivity of the copper precursor. This is achieved through efficient esterification catalysis by M^{3+} cations to produce M^{3+}-OH species, which then undergo hydroxide ligand transmetallation to form Cu^{+}-OH monomers (**Scheme 1**, bottom). These Cu^{+}-OH monomers then quickly condense to form Cu_2O NCs.

Spectroscopic data (UV-visible and FTIR) collected during and following the injection process provide detailed information about the formation of oleyl oleate ester and the consumption of the copper oleate (Cu^{2+}-O_2CR) precursor over time. These studies point to a new mechanism for metal oxide synthesis in which the generation of a metal oxide NC is not limited by the inherent reactivity of the parent metal (*i.e.* Cu) toward esterification to produce M-OH monomers. Instead, the monomers can be generated by transmetallation from a secondary M^{3+}-OH species produced from esterification catalyzed by a group 13 metal cation. These studies also highlight the competitive and independent reactivity of two metal cations in the same solution and are therefore important for the synthesis of more complex ternary metal oxide NCs.

Experimental

Materials Oleic acid (HO_2CR, R = $C_{17}H_{33}$, technical grade, 90%), and oleyl alcohol (HOR', R' = $C_{18}H_{35}$, technical grade, 80-85%) were purchased from Alfa Aesar and used as received. Copper (II) acetate ($Cu(OAc)_2$, 98%), indium (III) acetylacetonate ($In(acac)_3$, 99.99%), aluminum (III) acetylacetonate ($Al(acac)_3$, 99.99%), gallium (III) acetylacetonate ($Ga(acac)_3$, 99.99%) were purchased from Sigma-Aldrich and used as received. To monitor the nitrogen (99.999%, Airgas) flow rate, a Cole-Parmer flow meter (model PMR1-010270) was utilized. A syringe pump from New Era Pump Systems, Inc (Model NE-4000) was used to control injection rate.

General Synthesis of Copper(I) Oxide Nanocrystals To synthesize Cu_2O NCs, $Cu(OAc)_2$ (2.45 mmol) and 0, 1, 5, 10, or 15 mol% of $Al(acac)_3$, $Ga(acac)_3$, or $In(acac)_3$ was placed in a 25 mL 3-neck round bottom flask with 5 mL of oleic acid to result in a 0.49 M [$Cu(OAc)_2$] mixture. This flask was then capped with three rubber septa and the mixture was heated to 150 °C under nitrogen flow with constant stirring for thirty minutes to produce copper oleate precursor (Cu^{2+}-O_2CR) and the corresponding M^{3+}-O_2CR catalyst. This step also facilitates the removal of any acetic acid or acetylacetone through evaporation. In a separate 100 mL 3-neck round bottom flask, 25 mL of

oleyl alcohol was heated to 200 °C while nitrogen was flowed over the solvent. The precursor solution was allowed to cool to 90 °C before 4 mL of the solution (equivalent to 1.96 mmol of Cu^{2+}-O_2CR) was then drawn into a 10 mL syringe and injected into the oleyl alcohol at a rate of 0.35 mL min^{-1} using a syringe pump. The reaction flask was constantly stirred during and after injection and the solution was held at 200 °C for 5 minutes after the injection was completed. The flask was then removed from heat and slowly cooled to room temperature.

The reaction mixture was centrifugated at 7500 rpm for 10 minutes to separate the solid product and supernatant. The supernatant was collected for further spectroscopic analysis. The solid was washed using 15 mL of hexanes and sonicated using an ultra-sonication horn (Branson 150) for resuspension. An equal volume of acetone was added to precipitate particles in solution. This was followed by centrifugation at 7500 rpm for 5 minutes. The washing and centrifugation steps were repeated 3 times. The resulting solid was dried from acetone in a vacuum oven for characterization. Solid isolation and washing were performed under ambient conditions.

Characterization of Copper(I) Oxide Nanocrystals and Post-Reaction Solutions Solid state materials resulting from the synthesis were characterized using multiple techniques. Powder X-ray diffraction (PXRD, Rigaku SmartLab, Cu Kα) was used to assess phase and crystallinity of the synthesized materials. Diffractograms were collected and compared to a Cu_2O standard (PDF #01-078-2076). Scanning electron microscopy (SEM, Hitachi S-4700 Field Emission Microscopy) and transmission electron microscopy (TEM, Thermofisher Talos F200X, lacey carbon on gold TEM grid) were used to assess particle size and morphology. Elemental composition was determined using Inductively Coupled Plasma – Mass Spectrometry (ICP-MS, Agilent 7900 Quadrupole) and Energy Dispersive Spectroscopy (EDS, Super-X EDS attached to TEM).

The post-reaction solution (*i.e.* supernatant from initial centrifugation) was characterized to understand the extent of reactivity with each M^{3+} catalyst using attenuated total reflectance Fourier transform infrared (ATR-FTIR) spectroscopy (Nicolet iS-50 with built-in ATR) and UV-visible absorbance spectroscopy (Agilent Cary 5000, thin path length (0.2 cm) glass cuvette). For ATR-FTIR measurements, a liquid drop of post-reaction solution was place directly on diamond ATR crystal.

Time Dependent Copper(I) Oxide Synthesis For kinetic analysis of the Cu_2O synthesis, the reaction was performed as described above, but with small aliquots (100-200 μL) removed from the reaction approximately every thirty seconds during the injection period, and every minute after

the conclusion of the injection period. These aliquots were analyzed via ATR-FTIR by directly adding liquid drops of each aliquot on the ATR crystal. UV-visible absorbance measurements for the aliquots were collected by diluting 100 μL of aliquot with 900 μL of oleyl alcohol.

Results and Discussion

Cu_2O Synthesis Cu_2O nanocrystals were synthesized by a continuous-injection procedure. $Cu(OAc)_2$ and the appropriate $M(acac)_3$ salt were first combined in oleic acid (HO_2CR, R= $C_{17}H_{33}$) and heated at 150 °C for a minimum of 30 minutes to generate Cu^{2+}-O_2CR and M^{3+}-O_2CR species. The amount of Cu^{2+}-O_2CR, also referred to as the precursor, used for each experiment was constant at 1.96 mmol. The concentration of M^{3+}-O_2CR catalysts, also referred to as M^{3+}, were varied based on mol% of the precursor. 4 mL of the prepared precursor/catalyst solution was then injected at a controlled rate of 0.35 mL/min into oleyl alcohol at 200 °C. After completion of the injection, the temperature was held at 200 °C for 5 minutes to allow for the reaction of any remaining precursor before the flask was removed from the hot plate and allowed to slowly cool to room temperature. Solid products were isolated from the final solution following multiple washing/extraction steps.

Figure 1a shows PXRD data collected for solid products resulting from 10 mol% Al^{3+}, Ga^{3+}, and In^{3+}, compared with 0 mol% catalyst. PXRD data for all catalyst conditions are shown in **Figure S1**. For Ga^{3+} and In^{3+} reactions, Cu_2O is the exclusive product with no evidence of side products such as CuO or M_2O_3. For some reaction conditions, Cu^0 was produced as a minor product. Conditions which favored the production of Cu^0 included elevated temperatures (>215 °C, **Figure S2**), slow injection rates, and extended times following injection at which the reaction remained at high temperature. We also note that Cu^0 was produced for >5 mol% Al^{3+} (**Figure S1**). The Cu_2O observed when Cu^0 metal was present was green in color, as opposed to the yellow/orange solid produced when no Cu^0 was present. The green colored solid has been attributed to a Cu^0 core with a Cu_2O shell.[20]

The fact that Cu_2O is observed instead of CuO indicates that oleyl alcohol acts as a sufficient reductant for the conversion from Cu^{2+} to Cu^+ during the reaction. Evidence for alcohol reduction of copper has previously been reported in the literature.[21] Given that CuO is not produced in any detectable quantity, we also believe that copper reduction occurs prior to nanocrystal formation such that Cu_2O is formed directly from Cu^+-OH monomers. In fact, if the reaction temperature was held below 200 °C, no solid formation occurred and the reaction solution stayed green in color,

indicating that Cu^{2+} was never reduced (**Figure S3**). Attempts to use a Cu^{+} precursor (*i.e.* Cu(OAc)) as a starting material were unsuccessful, as the exchange of acetate and oleate ligands oxidized Cu^{+} to Cu^{2+} with the resulting precursor solution having the same absorbance spectrum and color as Cu^{2+}-O_2CR (**Figure S4**).

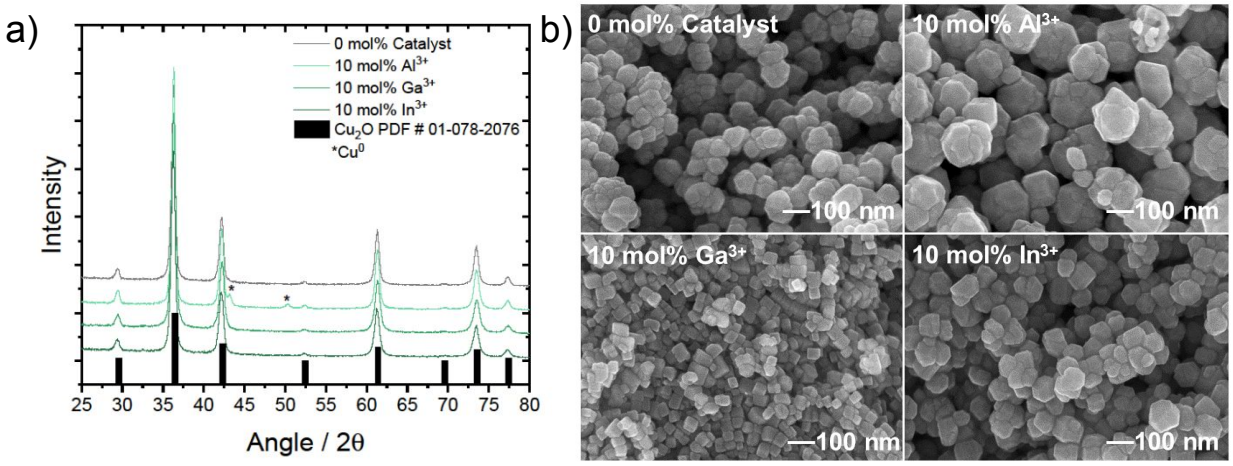

Figure 1. a) PXRD data collected for Cu_2O NCs synthesized by continuous-injection of Cu^{2+}-O_2CR as a function of 0 mol% and 10 mol% Al^{3+}, Ga^{3+}, or In^{3+} catalyst loading at 200 °C under N_2. A standard diffraction pattern for Cu_2O (PDF# 01-078-2076) is shown for comparison. b) SEM images of Cu_2O NCs synthesized in the absence (0 mol%) and presence of 10 mol% M^{3+} catalysts.

In terms of M^{3+} oxide side products, we note that the synthesis of In_2O_3 has been heavily explored with the continuous-injection method.[8–11,16,22] However, the low concentrations of In^{3+} used in these studies does not yield In_2O_3 product. For example, control experiments using only M^{3+}-O_2CR up to 0.30 mmol (equivalent to 15 mol% catalyst loading) showed no solid formation for any of the group 13 metal cations. However, injection of In^{3+}-O_2CR and Ga^{3+}-O_2CR at 2 mmol (equivalent to 100 mol% catalysts loading) did yield nanocrystalline In_2O_3 and γ-Ga_2O_3 (**Figure S5**). Similar experiments for Al^{3+} at 100 mol% were unsuccessful, as the precursor solidified in the syringe at high concentrations, making it impossible to inject.

SEM images of NCs produced with 0 mol% catalyst and 10 mol% Al^{3+}, Ga^{3+}, or In^{3+} are shown in **Figure 1b**. SEM images for 1, 5, and 15 mol% catalysts are shown in **Figure S6**. NC sizes for different mol% are given in **Table 1** and **Figure S7**. With no catalysts present, Cu_2O NCs were found to be roughly spherical with minor faceting and an average size of 129 ± 27 nm. NC agglomeration was also observed and believed to be due to weak coordination of oleate ligands to

the Cu_2O surface. This observation was consistent across all reaction conditions. As a function of M^{3+} catalyst, clear differences in the size and morphology of Cu_2O NCs were observed. In general, the size of NCs was found to increase in the order $Ga^{3+} < In^{3+} < Al^{3+}$. Cu_2O produced from Ga^{3+} also exhibited a distinct cubic morphology while NCs resulting from In^{3+} and Al^{3+} were more spherical in shape, similar to those produced in the absence of M^{3+} cations. The change in the morphology with the addition of Ga^{3+} specifically points to a unique change in the kinetics of Cu_2O formation discussed further below. For all M^{3+} cations, no significant trends were observed between NC size and mol% catalyst. TEM images for all reaction conditions are shown in **Figure S8-S16**. ICP-MS analysis (**Table S1**) showed that the percentage of each catalyst metal with respect to copper never rose above 0.8 % even for higher mol% catalyst conditions. We believe this is a strong indication that Al^{3+}, Ga^{3+}, and In^{3+} are not incorporated into the Cu_2O solid as dopants. Although EDS is less quantifiable, measurements performed in combination with TEM also did not indicate the presence of In, Ga, or Al atoms within individual Cu_2O NCs (**Figure S17**).The detected quantities of catalyst metals from ICP-MS are therefore likely due to residual M^{3+}-O_2CR present within the oleate ligand shell.

Table 1. Cu_2O NC sizes (nm)

No Catalyst	**0 mol%**			
Cu^{2+}-O_2CR	129 ± 27			
With Catalyst	**1 mol%**	**5 mol%**	**10 mol%**	**15 mol%**
Al^{3+}	169 ± 30	96 ± 15	191 ± 22	168 ± 43
Ga^{3+}	62 ± 11	64 ± 13	58 ± 13	72 ± 16
In^{3+}	111 ± 19	117 ± 17	90 ± 17	85 ± 14

Despite the noted changes in Cu_2O NC size and morphology with M^{3+} cations, it is not apparent from PXRD or microscopy data that these metals are acting catalytically for Cu_2O formation. However, UV-visible absorbance and FTIR spectroscopy provide compelling evidence for this assignment and offer new insights into possible mechanisms for metal oxide formation. **Figure 2** shows UV-visible absorbance spectra obtained from post-reaction solutions for each catalyst. These spectra show a peak at 695 nm consistent with the Cu^{2+}-O_2CR precursor. The 0 mol% condition resulted in post-reaction solutions which are deep green in color due to the strong peak

at 695 nm. As catalysts were introduced, the intensity of the green color diminished as the peak decreased, finally resulting in a yellow amber color as the peak completely disappeared.

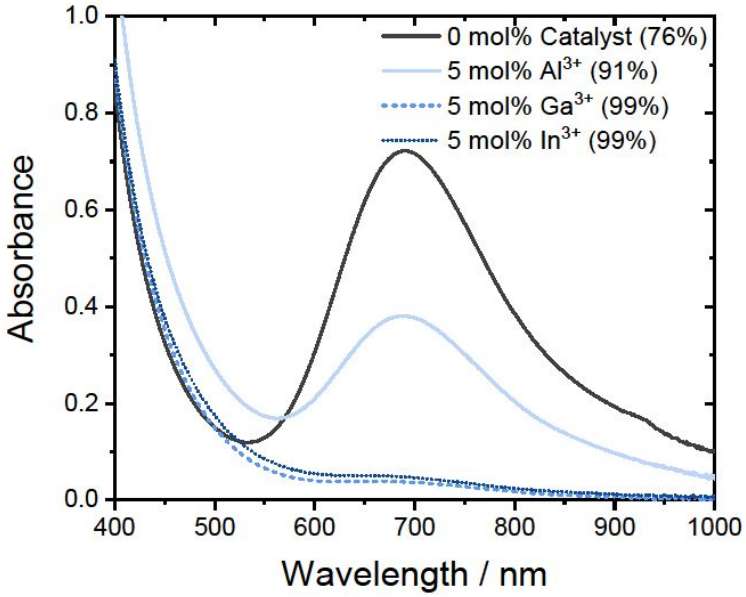

Figure 2. UV-visible absorbance spectra of post-reaction solutions obtained from continuous-injection of Cu^{2+}-O_2CR with 0 mol% and 5 mol% Al^{3+}, Ga^{3+}, or In^{3+} at 200 °C under N_2. The peak at 695 nm is indicative of unreacted Cu^{2+}-O_2CR precursor remaining in solution. Absorbance was corrected for oleyl alcohol.

The magnitude of the 695 nm peak in the post-reaction solution can be used to measure reaction efficiency with the equation $\eta_{rxn} = 1 - [Cu^{2+}]_{unreacted}/[Cu^{2+}]_{total}$. The concentration of unreacted precursor was calculated for these solutions based on the extinction coefficient of the 695 nm peak (**Figure S18**). In the case of 0 mol% catalyst, $[Cu^{2+}]_{unreacted} = 17$ mM, resulting in $\eta_{rxn} = 76\%$ based on a $[Cu^{2+}]_{total} = 68$ mM present in the oleyl alcohol/oleic acid solution after injection. Upon addition of 5 mol% Al^{3+}, Ga^{3+}, or In^{3+}, $[Cu^{2+}]_{unreacted}$ decreased to 8.2, 4.4, and 5.9 mM, corresponding to $\eta_{rxn} = 86$, 99, and 98%, respectively. In the case of Al^{3+}, the 695 nm peak remained present for all mol% catalyst conditions, indicating incomplete reactivity. $[Cu^{2+}]_{unreacted}$ was never less than 7 mM with the addition of up to 15 mol% Al^{3+}, resulting in a maximum $\eta_{rxn} = 90\%$. (**Figure S19**) With Ga^{3+} or In^{3+}, η_{rxn} achieved >98% for ≥5 mol% catalyst loading.

Figure 3 shows a summary of FTIR spectra collected for post-reaction solutions as a function of mol% catalyst. Previous literature reports have used FTIR to evaluate the esterification reaction using peaks consistent with free oleic acid (1710 cm^{-1}), oleyl oleate ester (1738 cm^{-1}) and oleyl

alcohol (3300 cm^{-1}).[8] **Figure 3** clearly shows the presence of these species in addition to Cu^{2+}-O_2CR, identified by the C=O stretch of the bound oleic acid at 1620 cm^{-1}, and an unknown solvent peak at 1660 cm^{-1} likely due to impurity (notably, this peak was constant as a function of reaction conditions, indicating no reactivity in the esterification cycle). Based on FTIR data, all M^{3+} catalysts showed greater reactivity than Cu^{2+}-O_2CR for the conversion of oleic acid to oleyl oleate ester. Consistent with data from UV-visible absorbance, Al^{3+} showed little variation in ester formation as a function of mol% and incomplete consumption of Cu^{2+}-O_2CR (**Figure S20**). Ga^{3+} and In^{3+} both showed significant consumption of the oleic acid peak and the Cu^{2+}-O_2CR precursor in addition to formation of the ester peak.

Notably, these data were collected using an ATR-FTIR instrument, and while this is normally not a quantitative method, the low vapor pressure and high viscosity of the oleyl alcohol solvent allowed for a consistent sample volume to be obtained on top of the ATR crystal. Although we do not know the exact path length for the evanescent wave, Beer-Lambert plots of oleic acid (1710 cm^{-1}) and Cu^{2+}-O_2CR (1620 cm^{-1}) (**Figure S21-S22**) were found to be linear over the absorbance range shown in **Figure 3** and allowed for apparent extinction coefficients of ε_{app} = 0.16 M^{-1} and 0.56 M^{-1} to be estimated for each peak, respectively. In a separate experiment, the apparent extinction coefficient for oleyl oleate ester at 1738 cm^{-1} was determined to be ε_{app} = 0.20 M^{-1} by converting 100% of oleic acid molecules to oleyl oleate ester by heating to 230 ^{o}C in the presence of excess oleyl alcohol and no metal catalysts (**Figure S23**). These values allow for a reliable estimation of the concentrations of reactants and products for the esterification reaction which are discussed further below with respect to time-dependent FTIR experiments.

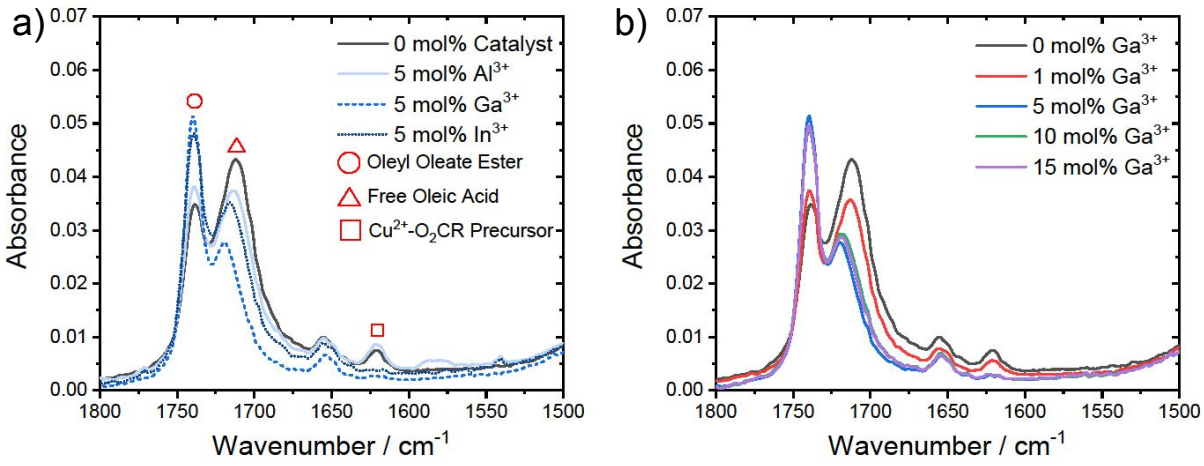

Figure 3. a) FTIR absorbance spectra in the C=O region of post-reaction solutions obtained from continuous-injection of Cu^{2+}-O_2CR with 0 mol% and 5 mol% Al^{3+}, Ga^{3+}, or In^{3+} at 200 °C under N_2. b) Similar data comparing 0-15 mol% Ga^{3+} catalyst loading conditions.

Time-Dependent Experiments The decrease in unreacted Cu^{2+} ions observed by UV-visible absorbance spectroscopy coupled with the enhanced production of oleyl oleate ester observed by FTIR points to a catalytic mechanism for the formation of Cu_2O in the presence of group 13 metals. To gain more insight, we performed time dependent experiments where 100-200 µL aliquots were removed from the reaction solution over a 17-minute time window. These aliquots were then analyzed by FTIR and UV-visible absorbance spectroscopy to observe the consumption of oleic acid and Cu^{2+}-O_2CR precursor while watching the evolution of oleyl oleate ester over time. **Figure 4** shows FTIR data for the reaction performed with 5 mol% Ga^{3+}. Similar data are shown in **Figure S24** for 0 mol% catalyst, 1 mol% Ga^{3+}, 10 mol% Ga^{3+}, 5 mol% Al^{3+}, and 5 mol% In^{3+} reactions. Note that data are plotted as ΔAbs with respect to the initial spectrum at 0 min, which represents an aliquot removed from the oleyl alcohol solution just before injection began. Over the course of 17 min, these data collectively show the consumption of oleyl alcohol (3300 cm^{-1}) concomitant with the growth of oleyl oleate ester (1738 cm^{-1}). Peaks associated with free oleic acid (1710 cm^{-1}) and Cu^{2+}-O_2CR precursor (1620 cm^{-1}) were found to increase initially as these species were injected into solution, but eventually decayed over time as the esterification reaction and consumption of Cu^{2+}-O_2CR progressed.

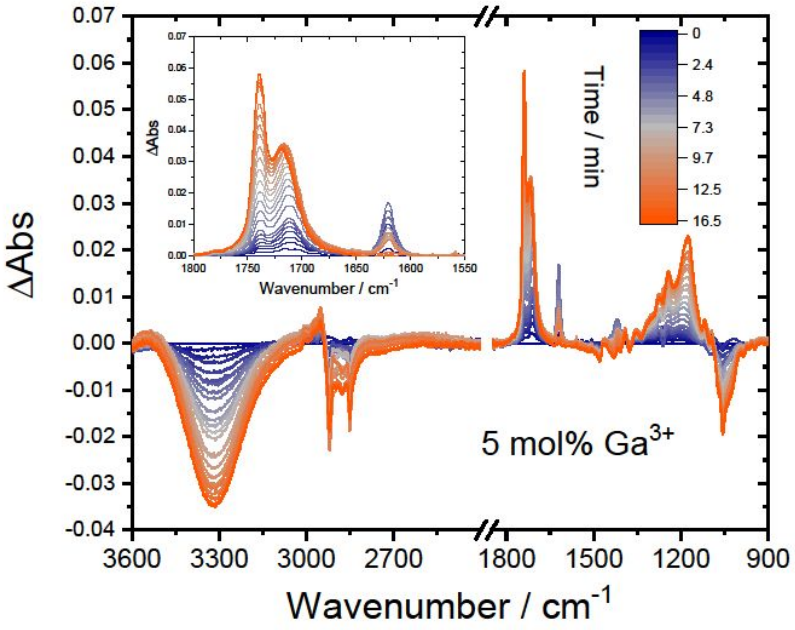

Figure 4. FTIR ΔAbs spectra collected for aliquots of reaction solution removed as a function of time during continuous-injection of Cu^{2+}-O_2CR with 5 mol% Ga^{3+} at 200 °C under N_2.

By analyzing changes in these peaks with respect to time we can see several trends that occur with each catalyst and mol%. **Figure 5a-b** show the Cu^{2+}-O_2CR precursor peak intensity at 1620 cm^{-1} as a function of time for different mol% Ga^{3+} and comparing 5 mol% for each group 13 metal. The rate for the initial buildup of precursor is consistent across all experiments due to the controlled injection rate of 0.35 mL/min, which is completed at the 11.5 min mark based on an injection volume of 4 mL. A 0 mol% catalyst injection performed at 25 °C is shown for comparison to highlight the rate of precursor growth and maximum concentration of precursor obtained in the absence of esterification or NC formation. Note that the measured maximum concentration of 75 mM represents a 10% increase from the expected concentration of 68 mM. This was a result of decreased volume from the ~25 aliquots removed from solution during the experiment. Across all reaction conditions, buildup of the precursor is shown to reach a critical limit before being consumed. The time point where consumption begins is consistent with where product formation is observed visually in the experiment as the solution changes from green to yellow. This was also confirmed by UV-visible absorbance spectroscopy by the peak observed at 490 nm, consistent with Cu_2O (**Figure S25**).[23] This time point was found to decrease from 9.2 min for 0 mol% Ga^{3+} to 5.5, 4.6, and 4.3 min for 1, 5, and 10 mol% Ga^{3+}, respectively. Among the group 13 metals, this

time point was found to decrease in the order Al^{3+} (8.9 min) < In^{3+} (4.9 min) < Ga^{3+} (4.6 min) for the 5 mol% condition.

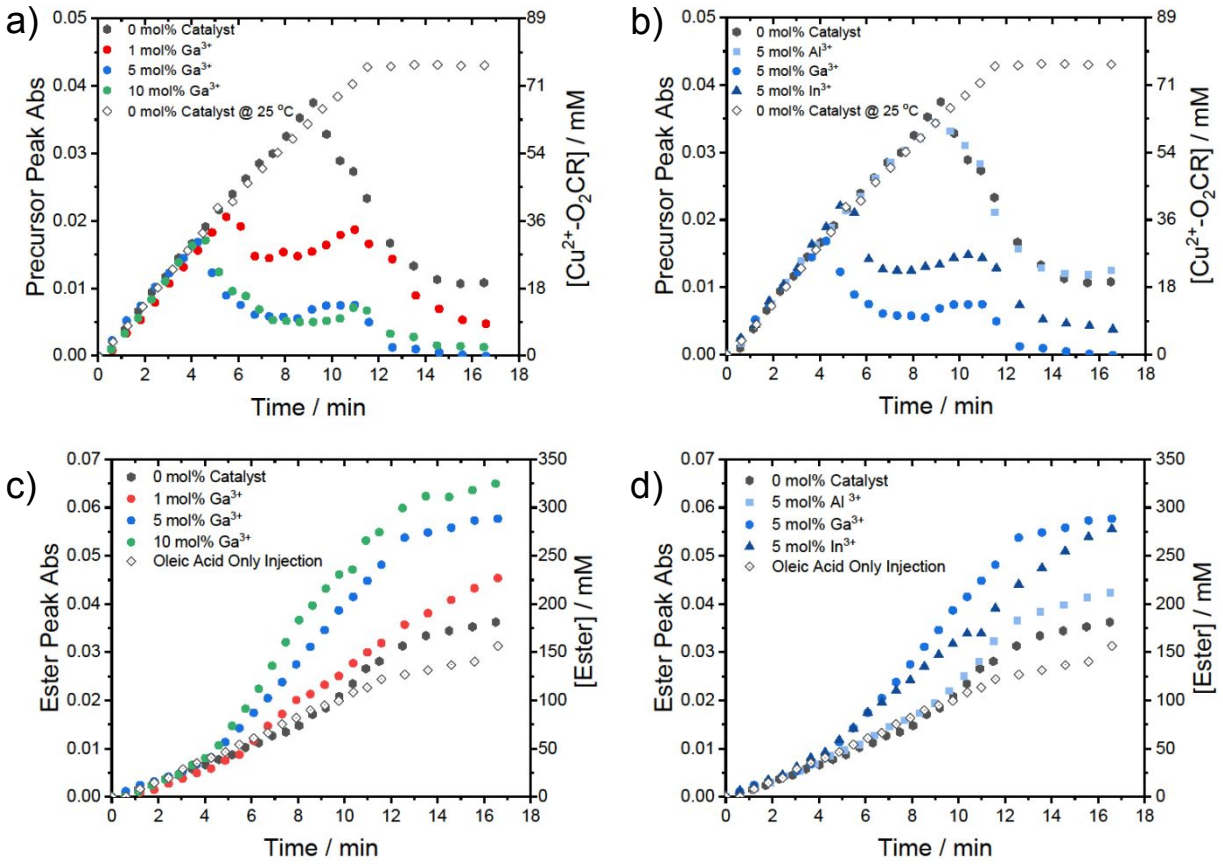

Figure 5. a-b) Precursor peak absorbance at 1620 cm^{-1} obtained from time-dependent FTIR measurements comparing 0-10 mol% Ga^{3+} and different group 13 cations at 5 mol%. c-d) Ester peak absorbance at 1738 cm^{-1} obtained from time-dependent FTIR measurements comparing 0-10 mol% Ga^{3+} and different group 13 cations at 5 mol%. Precursor and ester concentrations were calculated from apparent extinction coefficients obtained from **Figures S21-S23**.

In the cases of Ga^{3+} and In^{3+}, the precursor peak intensity reached steady-state around 7 min before rising again around 8-9 min and eventually decaying to lower values after 11 min. We believe this observation reflects the balance in rates between addition of the precursor/catalyst via injection and consumption via NC formation. Following the first decrease in precursor concentration, the rate of NC formation likely decreased with time and was equal to the injection rate around the 7 min mark. The rise in precursor around 8-9 min was therefore due to the rate of precursor consumption dropping below the rate of the injection, thus a net addition of precursor

was observed. When the injection was completed around 11 min, the precursor concentration decreased again because the rate of consumption was uncontested.

Figure 5c-d show time dependent FTIR data for the oleyl oleate ester peak intensity at 1738 cm^{-1}. Clear changes in the rate of ester formation are observed as a function of mol% Ga^{3+} and the nature of the group 13 metal. In all cases, the linear increase in Abs_{1738} between 0-4 min was due to background esterification as shown for the injection of oleic acid into oleyl alcohol at 200 °C in the absence of any metal (**Equation 1**, R = $C_{17}H_{33}$, R' = $C_{18}H_{35}$). The apparent rate for this background process was estimated to be 11 mM min^{-1} based on the linear slope from 0-11 min. The apparent zero-order nature of ester growth is likely due to the excess concentration of oleyl alcohol and the constant replenishment of oleic acid due to the slow injection rate. The total concentration of ester produced by **Equation 1** over the 17 min time window was found to be $[Ester]_{final}$ = 94 mM, equivalent to 24% conversion of injected oleic acid.

1) $H\text{-}O_2CR + R'\text{-}OH \rightarrow R'\text{-}O_2CR + H\text{-}OH$
2) $M\text{-}O_2CR + R'\text{-}OH \rightarrow R'\text{-}O_2CR + M\text{-}OH$

As the precursor/catalyst solution was injected, metal catalyzed esterification became an additional pathway for ester production (**Equation 2**), as indicated by the changes in rate observed at 10, 6, 4, and 4 min for 0, 1, 5, and 10 mol% Ga^{3+}, respectively. These time points were also found to coincide with the sharp decrease in the precursor peak, indicating that consumption of the precursor was triggered by metal catalysis. Furthermore, control experiments performed with 5 mol% Ga^{3+} in the absence of Cu^{2+}-O_2CR exhibited the same rate for ester formation and total ester produced as when Cu^{2+}-O_2CR was present (**Figure S26**), indicating that esterification is dominated by Ga^{3+} catalysis. The rates for metal catalyzed esterification were also found to be zero-order and were estimated to be 24, 20, 28, and 38 mM min^{-1} for 0, 1, 5, and 10 mol% Ga^{3+} based on the linear portion of ester growth immediately following the onset of metal catalysis. The $[Ester]_{final}$ produced also increased with mol% Ga^{3+} from 125 mM for 0 mol% to 183, 260, and 307 mM for 1, 5, and 10 mol%, respectively. These data indicate a clear dependence on $[Ga^{3+}]$ for the esterification reaction.

A comparison of group 13 metals at 5 mol% loading revealed that Al^{3+} catalyzed the esterification reaction only slightly better than Cu^{2+}-O_2CR on its own, with a rate of 27 mM min^{-1}

and $[Ester]_{final}$ = 163 mM (**Table 2**). The $[Ester]_{final}$ produced for Ga^{3+} (260 mM) and In^{3+} (247 mM) were much larger, but with comparable rates of 28 and 21 mM min^{-1}, respectively.

Turnover numbers (TON) for each catalyst were estimated by the equation TON = $[Ester]_{cat}/[Cat]$, where $[Ester]_{cat}$ (= $[Ester]_{final}$ - $[Ester]_{final(oleic\ acid)}$) is the concentration of ester produced by each catalyst and [Cat] is the total concentration of each metal ion in the reaction solution following injection. For example, at the 5 mol% condition, $[Cu^{2+}]$ = 75 mM and $[M^{3+}]$ = 3.8 mM. Resulting TON's showed that Ga^{3+} was the best group 13 catalyst with 44 ester molecules produced for every Ga^{3+} cation while Cu^{2+} achieved only 0.4 turnovers. Furthermore, TON was found to decrease with higher mol% for the Ga^{3+} series, showing that while the ester formation rate increased with more Ga^{3+}, not all cations were catalytically active. This will be discussed in detail further below.

Table 2. Comparison of M^{3+} Esterification Catalysis

Reaction Condition	η_{rxn}[a] (%)	Ester Rate[b] (mM min^{-1})	$[Ester]_{final}$[c] (mM)	$[Ester]_{cat}$[d] (mM)	TON[e]
Oleic acid only	-	11	94	-	-
Cu^{2+}-O_2CR	76	24	125	31	0.4
1 mol% Ga^{3+}	94	20	183	89	119
5 mol% Ga^{3+}	99	28	260	166	44
10 mol% Ga^{3+}	99	38	307	213	28
5 mol% Al^{3+}	86	27	163	69	18
5 mol% In^{3+}	98	21	247	153	41

[a]η_{rxn} = 1 - $[Cu^{2+}]_{unreacted}/[Cu^{2+}]_{total}$; [b]Estimated by the linear slope for growth of 1738 cm^{-1} FTIR peak; [c]$[Ester]_{final}$ = $(Abs_{final}(1738\ cm^{-1}) - \varepsilon_{app,acid}[Acid]_{total})/(\varepsilon_{app,ester} - \varepsilon_{app,acid})$ where $\varepsilon_{app,acid}$ = 0.04 M^{-1}, $\varepsilon_{app,ester}$ = 0.20 M^{-1}, and $[Acid]_{total}$ = 393 mM; [d]$[Ester]_{cat}$ = $[Ester]_{final}$ – $[Ester]_{final(oleic\ acid)}$; [e]TON = $[Ester]_{cat}/[Cat]$.

Catalytic Mechanism Based on the established mechanism of M-OH condensation to yield metal oxide NCs, we can reason that every copper ion present within Cu_2O must have existed as a Cu^{+}-OH monomer. The generation of these monomers could arise through copper catalyzed esterification like that shown in **Equation 2** or, as we propose here, transmetallation with M^{3+}-OH species. Unfortunately, we were unable to identify a unique FTIR absorbance resulting from the M^{3+}-OH bond, therefore we use the ester peak as an indirect measure of M^{3+}-OH formation. The

large $[Ester]_{cat}$ observed for Ga^{3+} and In^{3+} indicate that Ga^{3+}-OH and In^{3+}-OH are produced in high quantities. Based on **Equation 2**, the total moles of M^{3+}-OH produced over the lifetime of the reaction should be equal to the total moles of ester produced by the catalyst. Many of these M^{3+}-OH species are converted back to M^{3+}-O_2CR by reacting with oleic acid (**Equation 3**) whereby the catalyst is regenerated and may proceed through another cycle. However, in the presence of Cu^{+}-O_2CR, the transmetallation reaction shown in **Equation 4** could equally regenerate the M^{3+}-O_2CR catalyst while also producing Cu^{+}-OH. Here, we indicate Cu^{+}-O_2CR because the reaction does not proceed unless reduction of Cu^{2+} to Cu^{+} occurs. Therefore, we believe that the Cu^{2+}-O_2CR precursor is first reduced to Cu^{+}-O_2CR prior to transmetallation of the -OH ligand.

3) $H\text{-}O_2CR + M^{3+}\text{-}OH \rightarrow M^{3+}\text{-}O_2CR + H\text{-}OH$
4) $Cu^{+}\text{-}O_2CR + M^{3+}\text{-}OH \rightarrow M^{3+}\text{-}O_2CR + Cu^{+}\text{-}OH$
5) $Cu^{+}\text{-}O_2CR + H\text{-}OH \rightarrow H\text{-}O_2CR + Cu^{+}\text{-}OH$

It is important to note that **Equations 3-4** are the same reaction with the only difference being the nature of the cation bound to the -O_2CR ligand, H^{+} vs Cu^{+}. This comparison highlights the competition that exists between protons and metal cations for -OH ligands during the catalytic cycle. Control experiments which showed 5 mol% Ga^{3+} produced the same amount of ester with or without copper ions present suggest that their inclusion supplants H-O_2CR as a reactant with Ga^{3+}-OH.

While M^{3+}-OH species are suitable donors for -OH ligands, H_2O (H-OH) produced through background esterification or Cu^{+}-OH condensation could also deliver -OH ligands and bypass the copper catalyzed esterification route (**Equation 5**). In fact, it is known that if H_2O is not efficiently removed from solution during the synthesis of In_2O_3, then uncontrolled NC growth is observed through ligand exchange of In^{3+}-O_2CR and H_2O to generate In^{3+}-OH species.[8] From **Table 2**, it is apparent that a significant amount of Cu^{+}-OH must be generated by ligand exchange between Cu^{+}-O_2CR and H_2O. This is evident by the fact that TON = 0.4 but η_{rxn} = 76% for the 0 mol% condition. This means that, on average, only 40% of the copper ions go through one esterification cycle to produce Cu^{+}-OH, yet 76% of copper ions are consumed to produce Cu_2O. Notably, the reaction is designed to sweep H_2O from the reaction flask due the elevated temperature (200 ^{o}C) and continuous flow of N_2 over the solution surface. Based on **Equation 5**, it could even be possible

that the copper precursor does not catalyze esterification at all, and instead, the late onset for precursor consumption could be related to a slow buildup of H_2O in solution until a critical concentration is reached.

Scheme 2 provides two catalytic cycles to summarize our proposed reactions, with and without M^{3+} catalysts. In the presence of these catalysts, M^{3+}-O_2CR is able to catalyze the formation of oleyl oleate ester (R'-O_2CR) in the presence of oleyl alcohol (R'-OH) to produce M^{3+}-OH species. Likewise, Cu^{+}-O_2CR is able to catalyze the esterification reaction to produce Cu^{+}-OH. Given that copper catalysis is observed to be less efficient than M^{3+} catalysis, we believe that most, if not all, Cu^{+}-OH species are generated through transmetallation of -OH from M^{3+}-OH to Cu^{+}-O_2CR, defined by the central path. Once Cu^{+}-OH species are formed, rapid condensation occurs to produce Cu_2O NCs. Importantly, the condensation of M^{3+}-OH species is in direct competition with transmetallation and therefore the low concentration of M^{3+} catalysts is critical in preventing condensation and achieving the -OH transfer step. In the absence of M^{3+} catalysts, a mirrored reaction cycle can be shown in which oleic acid (H-O_2CR) replaces the M^{3+}-O_2CR species and undergoes esterification to yield oleyl oleate ester and water (H-OH) as products. Similar to the M^{3+} cycle, water may transfer the -OH ligand to Cu^{+}-O_2CR to generate Cu^{+}-OH and trigger Cu_2O formation. However, unlike the M^{3+} cycle, the -OH transfer reaction is in competition with the removal of water from the solution by vaporization.

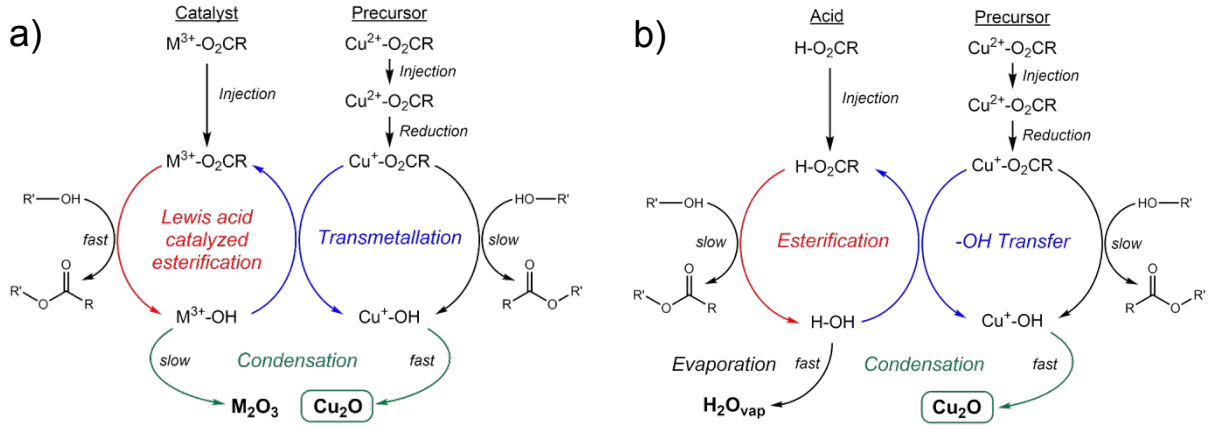

Scheme 2. a) Proposed catalytic cycle for M^{3+} catalyzed esterification to ultimately produce Cu_2O NCs through a -OH transmetallation step. b) Proposed catalytic cycle for the synthesis of Cu_2O NCs in the absence of M^{3+} catalysts.

Insights into Group 13 Catalysts Lewis acid catalyzed esterification is a well-studied reaction in the field of organic synthesis.[24–26] The established mechanism involves activation of the organic acid by coordination of the carbonyl group to the Lewis acidic cation, thus making the carbonyl carbon more susceptible to nucleophilic attack by an alcohol.[27] Therefore, the coordination environment around the metal as well its Lewis acidity play key roles in determining reactivity. Here, we have exchanged acetylacetonate ligands for oleate ligands with each group 13 metal to generate active catalysts. This was performed at elevated temperatures under inert gas; however, it is difficult to know the extent to which the ligand exchange reaction has been performed. This is especially important in the case of Al^{3+}. Among the group 13 metals, Al^{3+} is the strongest Lewis acid and would be expected to be the best catalysts for esterification.[28] However, here we observe it as the worst catalyst, barely better than the copper precursor. We believe this is due to incomplete exchange of the acetylacetonate ligands during preparation of the catalyst, which would result in catalytically inactive Al^{3+} cations. Indeed, Al^{3+} is the hardest acid and most oxophilic among the group and would therefore be expected to strongly resist ligand exchange from the chelated acetylacetonate environment.

Further evidence that incomplete preparation of the Al^{3+} precursor could be responsible for its lack of catalysis can be found by comparing the esterification rates for each catalyst with the reaction time in which metal catalysis begins. For all metals, including copper, the esterification rate was found to be within the range of 20-30 mM min^{-1}. However, Al^{3+} catalysis did not begin until 8.9 min for the 5 mol% condition compared to 4.6 min for Ga^{3+} and 4.9 min for In^{3+}. The slow reaction time onset could be the result of a low concentration of catalytically active Al^{3+} cations in the precursor solution which would need to build up in the reaction solution before the metal catalyzed esterification rate could be observed. This hypothesis is also predicated on the idea that a small amount of catalyst could maintain a high esterification rate.

Although we do not have mol% dependent data for Al^{3+}, we do have such data in the case of Ga^{3+}. Here, the esterification rate was found to increase with mol% catalyst; however, the TON decreased due to the fact that $[Ester]_{final}$ did not increase at the same rate as mol%. This observation suggests that only a small fraction of Ga^{3+} cations are driving the esterification reaction. Control experiments performed in which 100 mol% Ga^{3+} was present in the absence of Cu^{2+}-O_2CR, the esterification rate was found to be 23 mM min^{-1} and $[Ester]_{final}$ = 270 mM. This equates to a TON of 2.3. The low TON is the result of $[Ester]_{final}$ being roughly equal to that observed for 5-10 mol%

Ga^{3+} while the amount of catalyst was 10-20 times larger. One obvious reason for this is that a significant fraction of Ga^{3+}-OH species produced from each esterification cycle may undergo condensation with other Ga^{3+}-OH species to produce γ-Ga_2O_3. The condensation reaction would thus remove Ga^{3+} from the catalytic cycle and result in a lower amount of active catalysts. The same analysis can be performed with the 100 mol% In^{3+} condition in the absence of Cu^{2+}-O_2CR, resulting in an esterification rate of 19 mM min^{-1}, $[Ester]_{final}$ = 287 mM, and TON = 2.6.

The decrease in TON when going from 1 to 10 mol% Ga^{3+} may also be explained by competitive condensation which does not result in solid formation. Group 13 metals in aqueous solution are known to hydrolyze water to form μ-OH clusters.[29–31] When carboxylate ligands (*e.g.* acetate) are present, these clusters can also contain bridged carboxylates. In the case of Ga^{3+} and In^{3+}, oligomer chains of acetate ligands and metal cations have even been observed. It is therefore possible that μ-OH and μ-O coordinated Ga^{3+} clusters could result from condensation as the mol% is increased. This would thus lower the concentration of active Ga^{3+} cations for esterification. Notably, nucleation theory requires a critical concentration of monomers to be present in solution before nucleation may begin.[4] Below this threshold, the coalescence of monomers into larger clusters is thought to occur but that such structures are unstable and dissolve back into monomer units. Given the established literature of group 13 clusters with μ-OH and μ-O ligands, we believe these species may be long lived during the catalytic cycle. In fact, the formation of trinuclear μ-O clusters in the synthesis of Fe_2O_3 with the continuous-injection method have been observed and used to explain the continuous growth of NCs.[12]

Based on the metrics presented for esterification catalysis, In^{3+} appears to be comparable with Ga^{3+}, however, a clear distinction is made between the morphology and size of the resulting Cu_2O NCs. In the case of In^{3+}, NCs with diameters ≥85 nm were produced for all mol% conditions with spherical morphologies and a small degree of faceting. In the case of Ga^{3+}, resulting NCs were notably smaller (≤ 72 nm) and displayed a distinct cubic morphology across all mol% conditions. We believe the origin for this result must be related to the inherent reactivity of each metal towards esterification and transmetallation. **Figure 6** shows FTIR ΔAbs spectra in the C=O region for 100 mol% Ga^{3+} and In^{3+} injections in the absence of Cu^{2+}-O_2CR. While both metals catalyze esterification equally well, there is a notable difference in the observed absorbance features in the range of 1650 – 1500 cm^{-1}. This region displays peaks associated with the C=O bond of the M^{3+} bound oleate ligand. Interestingly, when the Ga^{3+}-O_2CR was injected into oleyl alcohol at 200 °C,

the precursor peak at 1563 cm^{-1} never grew in substantially during the reaction. In contrast, the In^{3+}-O_2CR peak grew in markedly during the injection period before decaying away upon condensation to form In_2O_3. Despite the Ga^{3+}-O_2CR peak not being significantly present during the catalytic reaction, nanocrystalline Ga_2O_3 was still produced (**Figure S5**).

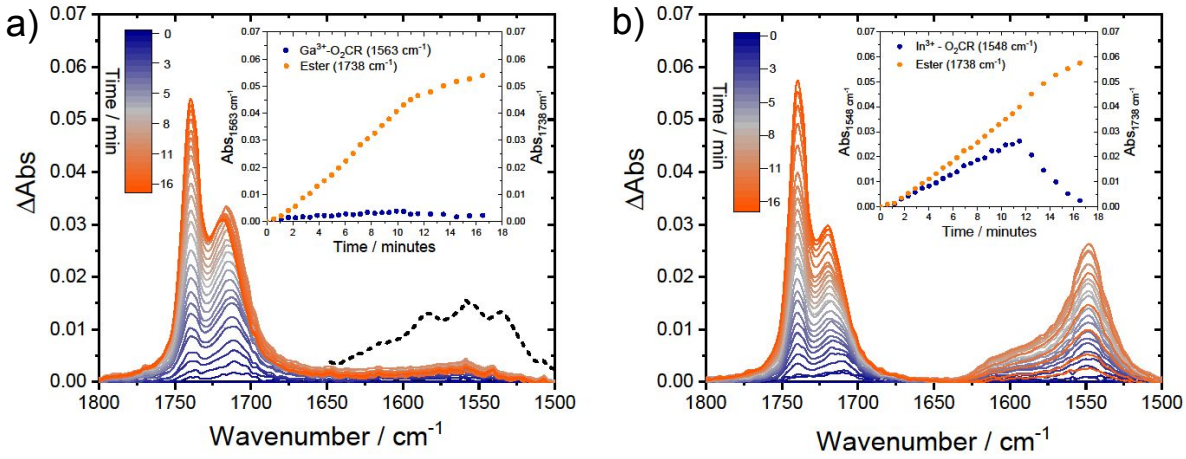

Figure 6. FTIR ΔAbs spectra for continuous-injection of 100 mol% a) Ga^{3+}-O_2CR and b) In^{3+}-O_2CR into oleyl alcohol at 200 °C under N_2. Insets for each figure show the precursor peak absorbance for M^{3+}-O_2CR and oleyl oleate ester measured over the course of the reaction. The dashed line spectrum shown in (a) is that of Ga^{3+}-O_2CR in oleyl alcohol at 25 °C for reference.

The absence of a precursor peak in the case of Ga^{3+} may be related to its ability to undergo condensation reactions to form μ-OH clusters. As discussed above, the mol% dependence for Ga^{3+} suggests that only a small fraction of Ga^{3+} cations are needed to maintain high levels of esterification. Indeed, the esterification rate and $[Ester]_{final}$ observed for 100 mol% Ga^{3+} were on par with those observed for 1-5 mol% Ga^{3+}. The propensity to form clusters may also be linked to the kinetics for transmetallation between Ga^{3+} and Cu^{+}, as transmetallation would necessarily involve the formation of a bimetallic μ-OH complex to facilitate -OH ligand transfer.

In the case of In^{3+}, the persistence of the In^{3+}-O_2CR peak could indicate slower reactivity toward condensation than Ga^{3+}. Fortunately, In_2O_3 synthesis and In^{3+} reactivity has been studied heavily by the Hutchison group[8,9,16,22] where one particular study focused on the impact of temperature and injection rate on In^{3+}-O_2CR precursor reactivity and the resulting morphology of In_2O_3 nanocrystals.[32] They show that at lower temperatures and/or fast injection rates the In^{3+}-OH

monomers are slower to react, causing branched nanocrystals to form, as opposed to at high temperatures and slower injection rates where spherical particles are observed. Our reaction conditions produced branched nanocrystals (**Figure S27)**, which Plummer *et al.* state is related to long-lived In^{3+}-OH monomers in solution. Such long lifetimes would imply slow kinetics for condensation and thus transmetallation to Cu^{+}.

Further evidence for the hypothesis of faster transmetallation kinetics for Ga^{3+} than In^{3+} can be found in the comparison of the 5 mol% catalyst data shown in **Figure 5**. In the case of Ga^{3+}, the time points at which the Cu^{2+}-O_2CR precursor peak decreased, associated with Cu_2O NC formation, and the onset for M^{3+} catalyzed esterification occurred were found to be identical at 4.3 min. In the case of In^{3+}, however, the decrease in the precursor peak (5.5 min) occurred 1.4 min after the onset of esterification (4.9 min). This lag in precursor consumption is a clear indication of transmetallation limited formation of Cu^{+}-OH monomers needed for Cu_2O formation. The rapid transmetallation of -OH ligands from Ga^{3+}-OH is therefore believed to be a significant factor in producing the cubic morphology observed for Cu_2O NCs.

Relevance to Metal Oxide Synthesis Many Cu_2O syntheses exist in the literature that give a variety of sizes and morphologies.[33–45] Early synthesis of small Cu_2O nanocrystals was achieved by oxidizing Cu^0 nanoparticles to Cu_2O in air.[46] This was characterized by a shift in color from metallic red to green. The green color of oxidized Cu^0 nanoparticles has been attributed to a Cu^0 core that remains buried beneath a Cu_2O shell.[20] Interestingly, Cu_2O that is synthesized directly (*i.e.* from Cu^{+}-OH monomers) is yellow/orange in color.[20,38,47] In most cases, our synthesis produced Cu_2O exclusively and through a direct route, but in the case of high temperature or with > 5 mol% Al^{3+} we produced Cu^0 nanocrystals, a small fraction of which turn green after oxidation in air, consistent with the literature.

Other syntheses which produced Cu_2O directly produce particles that are several hundred nanometers to microns in size and show impressive control over particle morphology.[37,40,45,48–52] The morphological change observed here with the addition of Ga^{3+} is consistent with the formation of nanocubes. In the literature, fast reactivity of precursors has been attributed with the cubic morphology whereas slower reactivity has resulted in octahedral NCs.[40] Only a few synthetic methods have been shown to produce small colloidal Cu_2O NCs.[20,23,38,47] These colloidal particles are capped with a variety of ligands including phosphate, amines, and carboxylates. The use of oleic acid in the continuous-injection method is necessary for the esterification reaction, but we

also believe that amines or thiols could better cap the Cu_2O NCs, preventing agglomeration and resulting in smaller particle size.[53,54]

We note that a recent report by Kim *et al.* described the effect of non-incorporative cations such as Na^+ and K^+ on the synthesis of In_2O_3 NCs where size and shape were effectively tuned.[11] These results were explained based on the concentration of free and bound oleate ligands, affected by [Na^+] and [K^+], and their influence of surface capping. In the present case, Ga^{3+} may exhibit similar effects to result in the nanocubic morphology of Cu_2O; however, we also believe that the rates of esterification by Ga^{3+}-O_2CR and transmetallation by Ga^{3+}-OH play significant roles to determine morphology.

To the best of our knowledge, this is the first report of a transmetallation mechanism for metal oxide synthesis. The observation of this mechanism in the present system relies on the competitive nature of metal catalyzed esterification and M-OH condensation reactions. Cu^+ appears to catalyze esterification slowly but undergo rapid condensation when Cu^+-OH monomers are formed. Ga^{3+} and In^{3+} possess fast catalysis for esterification while their condensation reactions can be inhibited through low mol% loadings. This sets up a reaction scheme where Cu^+ is able to bypass the esterification route and accept -OH ligands from M^{3+}-OH through transmetallation. This type of mechanism could unlock the ability to use metal cations which are not prone to catalyzing the esterification reaction on their own. Although the esterification method has been shown for a number of metals, some have shown resistance to this reactivity, including copper, silver, and antimony.[8] Furthermore, the inclusion of catalytic amounts of Ga^{3+} or In^{3+} into precursor solutions with other metals which are able to catalyze the esterification reaction (*i.e.* Fe, Co, Mn) may produce new reactivity through a more rapid production of -OH ligands in solution.

The possibility of transmetallation between two metal centers during the synthesis of metal oxides could also open the door to the preparation of new ternary oxide materials. For this to be achieved, the production M_1-OH and M_2-OH species would need to occur on the same timeframe and kinetics for cross condensation (*i.e.* M_1-OH + M_2-OH → M_1-O-M_2 + H_2O) would need to be faster than the formation of their respective binary oxides. The transmetallation step could even serve as a "buffer" to balance the rates of M_1-OH and M_2-OH production by transferring -OH ligands to the metal with a slower esterification rate. Indeed, the synthesis of some ternary oxide materials have already been reported in the literature using the continuous-injection method. However, these examples have centered on the synthesis of doped In_2O_3[9,16,22] where the dopant

metal occupies the same coordination environment and atomic position as In^{3+}. It is possible that transmetallation between metals plays a role in the synthetic mechanism for these materials but has not yet been identified. It remains to be seen if the continuous-injection method can be used to produce ternary oxide materials where each metal occupies a unique coordination environment. Notably, the formation of ternary oxides does not occur for the present reaction conditions. Even in the case of 1:1 Cu^{1+}:M^{3+} (the ratio for delafossite)[55–57] or 1:2 Cu^{2+}:M^{3+} (the ratio for spinel)[58], Cu_2O is always the major product. This speaks to a kinetic mismatch between the formation of Cu^{+}-OH and M^{3+}-OH species during the reaction.

Conclusion

Here we have shown a unique synthetic route for producing metal oxide NCs by the addition of group 13 Lewis acid catalysts to a continuous-injection methodology. Detailed time-dependent spectroscopic analysis reveals that the inclusion of these catalysts allow Cu^{+} to bypass the typical esterification route for production of Cu^{+}-OH monomers needed for Cu_2O formation. Instead, esterification is driven by the group 13 catalyst to form M^{3+}-OH species which then undergo transmetallation to form Cu^{+}-OH. Of the group 13 metals, we find that Ga^{3+} exhibits our "goldilocks" reactivity, resulting in the smallest NCs and a distinctive cubic morphology. The use of Lewis acids in this reaction scheme could allow for a greater versatility in binary and ternary metal oxide formation. Specifically, this strategy could be used to improve and/or modify the reactivity of metal precursors to generate unique materials. Further investigation of different metal-oleates and their reactivity with the continuous-injection method could allow for new syntheses to be developed for a wide variety of metal oxides.

Supporting Information

PXRD, SEM, TEM, EDS, UV-visible absorbance, and FTIR data.

Author Contributions

N.J.G. and A.R.C.B contributed equally. N.J.G., A.R.C.B, and B.H.F. designed the research plan. N.J.G., A.R.C.B., and N.C. performed the experiments. N.J.G., A.R.C.B., and B.H.F. wrote the manuscript.

Conflict of Interest

The authors declare no conflicts of interests.

Acknowledgements

The authors acknowledge support from the National Science Foundation, Division of Materials Research and EPSCoR through grant 1809847. A.R.C.B. acknowledges support from the Alabama Graduate Research Scholars Program funded through Alabama Commission for Higher Education and administered by Alabama EPSCoR. N.G. acknowledges support from an Undergraduate Research Fellowship awarded through the Office of Undergraduate Research at Auburn University. PXRD measurements were collected on a Rigaku SmartLab funded through the National Science Foundation, Division of Materials Research, Major Research Instrumentation program under grant 2018794. The authors thank Dr. Amar Kumbhar of the Chapel Hill Analytical and Nanofabrication Laboratory for assistance in collecting SEM, TEM, and EDS data as well as Dr. Zeki Billor of the Auburn University Department of Geosciences ICP-MS Lab facility for assistance in collecting ICP-MS data.

References

1 M. Cargnello, *Chem. Mater.*, 2019, **31**, 576–596.
2 Y. Yin and A. P. Alivisatos, *Nature*, 2005, **437**, 664–670.
3 J. E. Cloud, T. S. Yoder, N. K. Harvey, K. Snow and Y. Yang, *Nanoscale*, 2013, **5**, 7368–7378.
4 J. van Embden, A. S. R. Chesman and J. J. Jasieniak, *Chem. Mater.*, 2015, **27**, 2246–2285.
5 A. Agrawal, S. H. Cho, O. Zandi, S. Ghosh, R. W. Johns and D. J. Milliron, *Chem. Rev.*, 2018, **118**, 3121–3207.
6 V. K. LaMer and R. H. Dinegar, *J. Am. Chem. Soc.*, 1950, **72**, 4847–4854.
7 M. A. Wall, B. M. Cossairt and J. T. C. Liu, *J. Phys. Chem. C*, 2018, **122**, 9671–9679.
8 D. Ito, S. Yokoyama, T. Zaikova, K. Masuko and J. E. Hutchison, *ACS Nano*, 2014, **8**, 64–75.
9 A. W. Jansons and J. E. Hutchison, *ACS Nano*, 2016, **10**, 6942–6951.
10 A. W. Jansons, L. K. Plummer and J. E. Hutchison, *Chem. Mater.*, 2017, **29**, 5415–5425.
11 K. Kim, L. C. Reimnitz, S. H. Cho, J. Noh, Z. Dong, S. L. Gibbs, B. A. Korgel and D. J. Milliron, *Chem. Mater.*, 2020, **32**, 9347–9354.
12 H. Chang, B. H. Kim, H. Y. Jeong, J. H. Moon, M. Park, K. Shin, S. I. Chae, J. Lee, T. Kang, B. K. Choi, J. Yang, M. S. Bootharaju, H. Song, S. H. An, K. M. Park, J. Y. Oh, H. Lee, M. S. Kim, J. Park and T. Hyeon, *J. Am. Chem. Soc.*, 2019, **141**, 7037–7045.
13 L. K. Plummer and J. E. Hutchison, *Inorg. Chem.*, 2020, **59**, 15074–15087.

14 S. R. Cooper, L. K. Plummer, A. G. Cosby, P. Lenox, A. Jander, P. Dhagat and J. E. Hutchison, *Chem. Mater.*, 2018, **30**, 6053–6062.
15 P. Wainer, O. Kendall, A. Lamb, S. J. Barrow, A. Tricoli, D. E. Gómez, J. van Embden and E. Della Gaspera, *Chem. Mater.*, 2019, **31**, 9604–9613.
16 A. W. Jansons, K. M. Koskela, B. M. Crockett and J. E. Hutchison, *Chem. Mater.*, 2017, **29**, 8167–8176.
17 X. Li, H. Shen, J. Niu, S. Li, Y. Zhang, H. Wang and L. S. Li, *J. Am. Chem. Soc.*, 2010, **132**, 12778–12779.
18 L. Yi and M. Gao, *Cryst. Growth Des.*, 2011, **11**, 1109–1116.
19 T. Machani, D. P. Rossi, B. J. Golden, E. C. Jones, M. Lotfipour and K. E. Plass, *Chem. Mater.*, 2011, **23**, 5491–5495.
20 S. D. Pike, E. R. White, A. Regoutz, N. Sammy, D. J. Payne, C. K. Williams and M. S. P. Shaffer, *ACS Nano*, 2017, **11**, 2714–2723.
21 A. Singhal, M. R. Pai, R. Rao, K. T. Pillai, I. Lieberwirth and A. K. Tyagi, *Eur. J. Inorg. Chem.*, 2013, **2013**, 2640–2651.
22 B. M. Crockett, A. W. Jansons, K. M. Koskela, M. C. Sharps, D. W. Johnson and J. E. Hutchison, *Chem. Mater.*, 2019, **31**, 3370–3380.
23 M. Tariq, M. D. Koch, J. W. Andrews and K. E. Knowles, *J. Phys. Chem. C*, 2020, **124**, 4810–4819.
24 N. Mamidi and D. Manna, *J. Org. Chem.*, 2013, **78**, 2386–2396.
25 X. Hou, Y. Qi, X. Qiao, G. Wang, Z. Qin and J. Wang, *Korean J. Chem. Eng.*, 2007, **24**, 311–313.
26 T. Maki, K. Ishihara and H. Yamamoto, *Org. Lett.*, 2005, **7**, 5047–5050.
27 K. Ishihara, M. Nakayama, S. Ohara and H. Yamamoto, *Tetrahedron*, 2002, **58**, 8179–8188.
28 J. N. Bentley, S. A. Elgadi, J. R. Gaffen, P. Demay-Drouhard, T. Baumgartner and C. B. Caputo, *Organometallics*, , DOI:10.1021/acs.organomet.0c00389.
29 M. K. Kamunde-Devonish, D. B. Fast, Z. L. Mensinger, J. T. Gatlin, L. N. Zakharov, M. R. Dolgos and D. W. Johnson, *Inorg. Chem.*, 2015, **54**, 3913–3920.
30 Z. L. Mensinger, L. N. Zakharov and D. W. Johnson, *Inorg. Chem.*, 2009, **48**, 3505–3507.
31 M. Clausén, L.-O. Öhman, J. D. Kubicki and P. Persson, *J. Chem. Soc. Dalton Trans.*, 2002, 2559–2564.
32 L. K. Plummer, B. M. Crockett, M. L. Pennel, A. W. Jansons, K. M. Koskela and J. E. Hutchison, *Chem. Mater.*, 2019, **31**, 7638–7649.
33 S. Thoka, A.-T. Lee and M. H. Huang, *ACS Sustain. Chem. Eng.*, 2019, **7**, 10467–10476.
34 I. Mukherjee, S. K. Das, B. K. Jena, R. Saha and S. Chatterjee, *New J. Chem.*, 2018, **42**, 3692–3702.
35 X. Zhang, Y. Zhang, H. Huang, J. Cai, K. Ding and S. Lin, *New J. Chem.*, 2017, **42**, 458–464.
36 Q. Wang, Q. Kuang, K. Wang, X. Wang and Z. Xie, *RSC Adv.*, 2015, **5**, 61421–61425.
37 M. D. Susman, Y. Feldman, A. Vaskevich and I. Rubinstein, *ACS Nano*, 2014, **8**, 162–174.
38 A. Paolella, R. Brescia, M. Prato, M. Povia, S. Marras, L. De Trizio, A. Falqui, L. Manna and C. George, *ACS Appl. Mater. Interfaces*, 2013, **5**, 2745–2751.
39 Q. Li, P. Xu, B. Zhang, H. Tsai, S. Zheng, G. Wu and H.-L. Wang, *J. Phys. Chem. C*, 2013, **117**, 13872–13878.
40 W.-C. Huang, L.-M. Lyu, Y.-C. Yang and M. H. Huang, *J. Am. Chem. Soc.*, 2012, **134**, 1261–1267.

41 Q. Hua, D. Shang, W. Zhang, K. Chen, S. Chang, Y. Ma, Z. Jiang, J. Yang and W. Huang, *Langmuir*, 2011, **27**, 665–671.
42 K. X. Yao, X. M. Yin, T. H. Wang and H. C. Zeng, *J. Am. Chem. Soc.*, 2010, **132**, 6131–6144.
43 S. Sun, F. Zhou, L. Wang, X. Song and Z. Yang, *Cryst. Growth Des.*, 2010, **10**, 541–547.
44 Y. Sui, W. Fu, H. Yang, Y. Zeng, Y. Zhang, Q. Zhao, Y. Li, X. Zhou, Y. Leng, M. Li and G. Zou, *Cryst. Growth Des.*, 2010, **10**, 99–108.
45 C.-H. Kuo and M. H. Huang, *Nano Today*, 2010, **5**, 106–116.
46 M. Yin, C.-K. Wu, Y. Lou, C. Burda, J. T. Koberstein, Y. Zhu and S. O'Brien, *J. Am. Chem. Soc.*, 2005, **127**, 9506–9511.
47 X. Yuan, H. Yuan, L. Ye, J. Hu, Y. Xu and P. Li, *RSC Adv.*, 2015, **5**, 42855–42860.
48 A. V. Nikam, A. Arulkashmir, K. Krishnamoorthy, A. A. Kulkarni and B. L. V. Prasad, *Cryst. Growth Des.*, 2014, **14**, 4329–4334.
49 H. Shi, K. Yu, F. Sun and Z. Zhu, *CrystEngComm*, 2011, **14**, 278–285.
50 Y. Zhang, B. Deng, T. Zhang, D. Gao and A.-W. Xu, *J. Phys. Chem. C*, 2010, **114**, 5073–5079.
51 Y. Luo, S. Li, Q. Ren, J. Liu, L. Xing, Y. Wang, Y. Yu, Z. Jia and J. Li, *Cryst. Growth Des.*, 2007, **7**, 87–92.
52 C.-H. Kuo and M. H. Huang, *J. Phys. Chem. C*, 2008, **112**, 18355–18360.
53 D. R. Kauffman, P. R. Ohodnicki, B. W. Kail and C. Matranga, *J. Phys. Chem. Lett.*, 2011, **2**, 2038–2043.
54 A. Oliva-Puigdomènech, J. De Roo, J. Kuhs, C. Detavernier, J. C. Martins and Z. Hens, *Chem. Mater.*, 2019, **31**, 2058–2067.
55 B. R. Pamplin, T. Kiyosawa and K. Masumoto, *Prog. Cryst. Growth Charact.*, 1979, **1**, 331–387.
56 H. Kawazoe, M. Yasukawa, H. Hyodo, M. Kurita, H. Yanagi and H. Hosono, *Nature*, 1997, **389**, 939–942.
57 T. Omata, H. Nagatani, I. Suzuki, M. Kita, H. Yanagi and N. Ohashi, *J. Am. Chem. Soc.*, 2014, **136**, 3378–3381.
58 F. Conrad, C. Massue, S. Kühl, E. Kunkes, F. Girgsdies, I. Kasatkin, B. Zhang, M. Friedrich, Y. Luo, M. Armbrüster, G. R. Patzke and M. Behrens, *Nanoscale*, 2012, **4**, 2018–2028.